nature materials

LETTERS

PUBLISHED ONLINE: 29 MAY 2011 | DOI: 10.1038/NMAT3031

Direct tomography with chemical-bond contrast

Simo Huotari[1,2]*, Tuomas Pylkkänen[1,2], Roberto Verbeni[1], Giulio Monaco[1] and Keijo Hämäläinen[2]

Three-dimensional (3D) X-ray imaging methods have advanced tremendously during recent years. Traditional tomography uses absorption as the contrast mechanism, but for many purposes its sensitivity is limited. The introduction of diffraction[1–4], small-angle scattering[5–7], refraction[8–10], and phase[11–14] contrasts has increased the sensitivity, especially in materials composed of light elements (for example, carbon and oxygen). X-ray spectroscopy[15–19], in principle, offers information on element composition and chemical environment. However, its application in 3D imaging over macroscopic length scales has not been possible for light elements. Here we introduce a new hard-X-ray spectroscopic tomography with a unique sensitivity to light elements. In this method, dark-field section images are obtained directly without any reconstruction algorithms. We apply the method to acquire the 3D structure and map the chemical bonding in selected samples relevant to materials science. The novel aspects make this technique a powerful new imaging tool, with an inherent access to the molecular-level chemical environment.

The nature of the contrast is the most fundamental property of any imaging technique, giving each method its unique characteristics. For X-ray imaging, there are several interaction mechanisms of X-rays with matter that could be exploited as a contrast mechanism. The most prominent are X-ray absorption, emission and scattering. Scattering can be further divided into elastic and inelastic branches. The former is seen for example as diffraction, and the latter is measured by inelastic X-ray scattering (IXS) spectroscopy[20], which is a modern tool in many areas of the study of electronic structure and dynamics of materials. It provides information similar to electron energy-loss spectroscopy (EELS), as they both measure the so-called energy-loss function, $-\mathrm{Im}\,\varepsilon^{-1}(\mathbf{Q},E)$, where $\varepsilon(\mathbf{Q},E)$ is the dielectric function. The loss function depends on exchanged momentum $\mathbf{Q}$ and energy E. The energy-loss spectra reveal detailed information on the states and excitations of both valence and core electrons.

We have developed a novel three-dimensional (3D) X-ray dark-field imaging technique using high-resolution IXS of hard X-rays (10–20 keV) as contrast. The technique has most notably a unique sensitivity for low-Z ($Z < 10$) elements and their chemical bonding characteristics, including orbital orientations. One of the important differences between our technique and other 3D X-ray imaging methods is that it is a single-shot direct tomography (DT) as opposed to angle-scan reconstruction-based computed tomography (CT). The comparison is similar to that with magnetic resonance imaging (MRI), which is also a rotation-free tomographic technique with its own unique contrast mechanism and sensitivity to certain low-Z isotopes. As with MRI, the spatial resolution and statistical accuracy of our new scattering-based DT is currently inferior to that of traditional CT. However, both MRI and DT have unique aspects that make them attractive.

The principle of the experiment is shown in Fig. 1. First, for reference, Fig. 1a shows the principle of traditional 3D X-ray imaging. Whether the contrast is that of absorption, scattering, refraction, or phase shifts on scattering from interfaces, 2D projections (or scattering patterns) are taken with multiple angles between the sample and the source-detector axes. The 3D structure is only resolved after a reconstruction process. The new DT technique is shown in Fig. 1b. It is based on an off-axis optical component, namely a spherically curved analyser crystal, that selects a narrow energy bandwidth of radiation scattered by the sample and focuses it on the detector. The analyser observes scattering into a fixed scattering angle 2θ, which in our measurements was in the range $30° < 2\theta < 60°$. The selection of the bandwidth is based on Bragg's law[21]. Note that the technique results in dark-field[7] images by construction, as only scattering is measured—the undeflected direct beam is not observed in the experiment at all when 2θ is larger than the analyser aperture (typically $\pm 3°$).

The described new technique is a direct tomographic imaging method, as images of 2D sections (that is, not projections) from the interior of the sample are measured directly without needing to obtain multiple projections or apply any reconstruction algorithm, in a similar fashion to that in X-ray diffraction topography[22,23]. It is thus possible to concentrate on only an interesting section or path and measure, for example, its time evolution. Note that there is no requirement for the direct beam to actually be transmitted through the sample or its environment, as exemplified in another CT/DT comparison in Fig. 2a,b: DT requires only relatively small apertures for incident and scattered X-rays. This is highly advantageous when studying samples enclosed for example in furnaces or other opaque containers, which could pose problems for angle-scan CT but are important for *in situ* materials characterization. Obviously, if the sample is not sufficiently transparent throughout, then attenuation of the incident and/or scattered X-rays within the sample may prevent the acquisition of signals from certain subvolumes. However, such possibly occurring artefacts do not propagate to the signal obtainable from other parts of the sample, and can be avoided in a chosen region by orientating the sample appropriately.

Entirely new types of contrast methods become available within DT. They are related to the energy-loss spectrum, measured with a very high energy resolution, of the order of ~1 eV. A schematic example of the most important contrast methods available is shown in Fig. 2c. The measurements record the intensity at a selected energy transfer. For an energy transfer of zero the measurement corresponds to X-ray diffraction (or diffuse scattering for non-crystalline samples) tomography, using the static structure factor $S(\mathbf{Q})$ as the contrast; we will refer to this as diffraction contrast. The new contrast methods are offered by inelastic energy-loss processes, represented by the dynamic structure factor $S(\mathbf{Q},E)$. The inelastic processes include scattering from phonons, valence-electron excitations, plasmons, and Compton scattering (Fig. 2c; ref. 20).

As the contrast mechanism, here we chose IXS from core-electron excitations; that is, the process called X-ray Raman scattering (XRS; refs 20,24–26), a rapidly developing tool that gives

[1]European Synchrotron Radiation Facility, BP 220, F-38043 Grenoble, France, [2]Department of Physics, University of Helsinki, PO Box 64, FI-00014 Helsinki, Finland. *e-mail: simo.huotari@helsinki.fi.

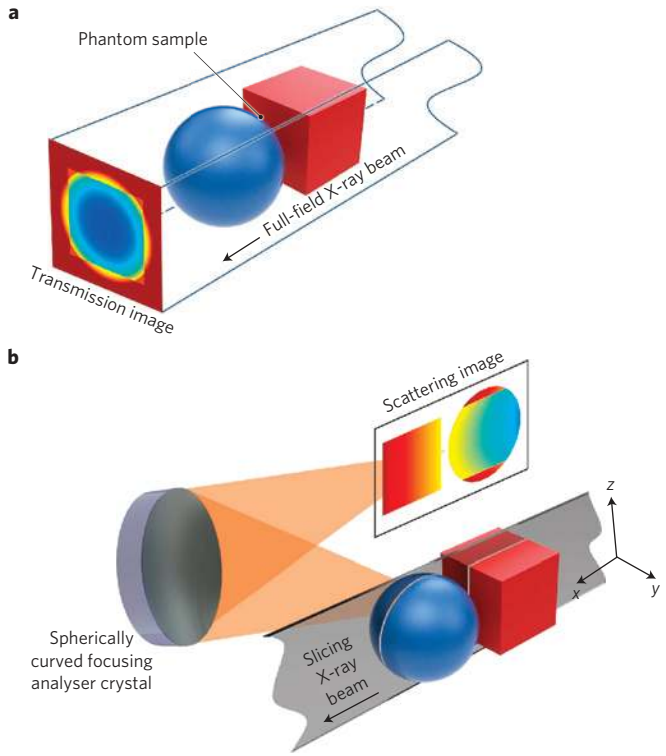

Figure 1 | The principle of the experiment. a, Typical 3D imaging technique measures 2D projections of the sample, which are collected for many orientations. A 3D image of the sample is then obtained via a reconstruction algorithm. **b**, In direct tomography, 2D sections in the *xz* plane are collected directly with a single shot. Any point in the X-ray-illuminated 2D section of the sample is projected on a unique point on the detector. The 3D structure can be mapped by scanning the sample over the remaining Cartesian dimension *y*.

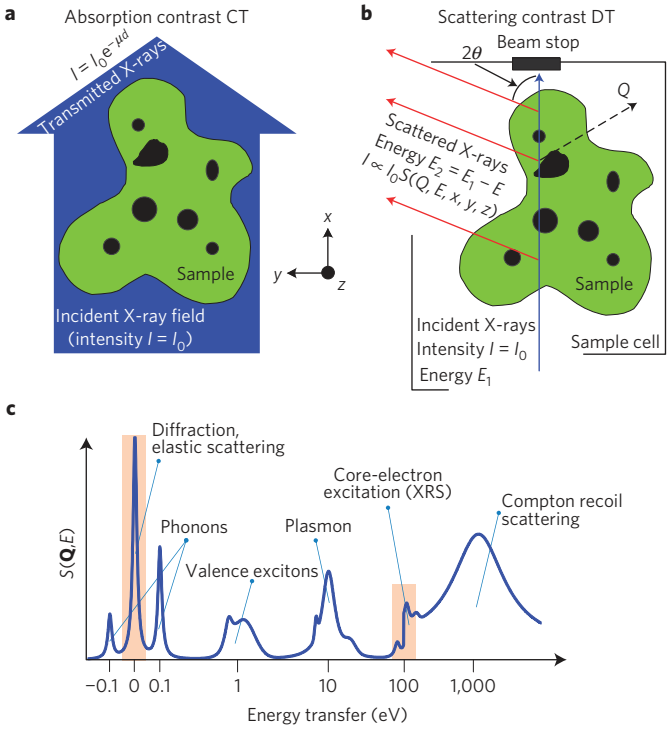

Figure 2 | Scattering-based direct tomography. a, Absorption-contrast CT gives information on the variation of the absorption factor μd within the sample's internal structure. **b**, Scattering-based DT gives information on the scattering factor $S(\mathbf{Q}, E)$ of the parts of the sample illuminated by the incident X-ray beam. Note that in DT only relatively small viewport apertures to the sample are needed, as exemplified by the sample cell walls in the figure. **c**, Schematic IXS spectrum showing the different excitations that can be used as the DT contrast mechanism. In this Letter, we use elastic scattering and XRS (highlighted) as contrasts.

information similar to X-ray absorption spectroscopy (XAS). In XRS the energy transfer plays the role of the absorbed-photon energy of XAS. The incident-photon energy can be chosen freely. This makes it possible to measure soft-X-ray absorption edges (such as the C *K*-edge at 290 eV, or the O *K*-edge at 535 eV) with hard X-rays. The XRS spectra yield information on the local structure and chemical bond of the specific element. In XRS the limitations of soft-X-ray spectroscopies are lifted; most importantly the XRS technique is bulk sensitive in many samples up to the millimetre or even centimetre scale (the probing depth for 13-keV X-rays in graphite is 6 mm). As vacuum conditions are not necessary, liquid and wet samples can be used, which is necessary for many biological studies. Our measurements were done by first rapidly mapping 3D volumes using diffraction contrast, and then concentrating on interesting regions using the XRS contrast, which constituted the slower part of the experiments.

As the DT measurements take place naturally in the Cartesian space, the spatial resolutions in the x, y, z directions are independent. In our notation, x is the direction along the incident X-ray beam (Fig. 1b). We have developed two different scanning modes for the DT experiment with slightly different characteristics. In the fast 2D sectioning mode, the incident beam can be prepared by focusing only in the y direction, leaving it unfocused in the z direction. In this case the imaging in the xz plane is left to the analyser crystal, and one can illuminate a large section of the sample at once. This is the direct 2D xz section, hence the name, direct tomography. Note that, to obtain this section, there is no movement of the sample, the beam, or the detector involved. To change the slice illuminated by the beam, the sample is moved in y. The thickness of the measured section is determined by the focus of the incident beam, and the analyser/detector combination gives the spatial resolution in the xz plane. In the high-resolution 1D piercing mode, the incident beam is focused in both y and z directions, resulting in a 1D piercing pathway through the sample. In this case the spatial resolution in y and z is determined by the incident-beam focus and in the x direction by the analyser. Here, the 3D volume is measured by a mesh scan over y and z. This method is slower than the 2D sectioning method, but interesting because of the currently better achievable spatial resolution.

To demonstrate the chemical-bond contrast for materials science applications, here we chose two examples. As a well-characterized phantom, we used a diamond buried inside a pellet compressed from graphite powder. In this sample (Fig. 3a), by using the chemical-bond contrast, we expect to be able to discriminate not only the diamond from the graphite by its different carbon bond, but also to determine the graphite orientation. First, to get a general overview of the sample, we measured the 3D volume around and including the diamond using DT with diffraction contrast corresponding to the [220] Debye–Scherrer ring of graphite, with the result shown in Fig. 3b. Diffraction contrast is naturally able to discriminate the two carbon forms here because of their different crystal structures. However, more interesting is that the chemical bond (in this case, sp^2 versus sp^3) can be determined for each voxel using XRS as a contrast. The C *K*-edge XRS spectra of diamond and graphite are very different because of the different nature of the sp^2 and sp^3 bonds. This is exemplified in the measured fingerprint spectra from highly oriented pyrolythic graphite and diamond powder (Fig. 3c). A determination of the intensities at

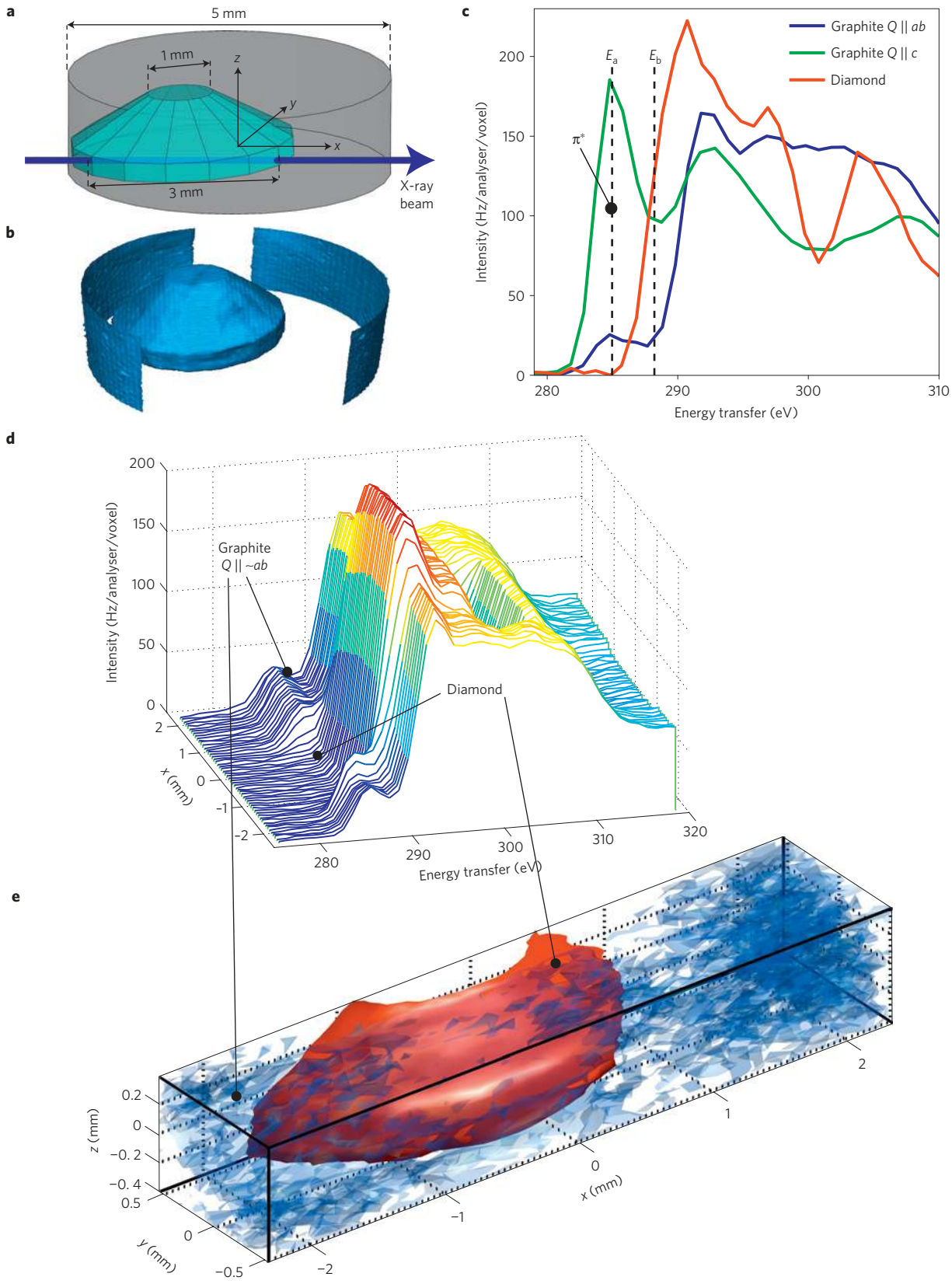

Figure 3 | Direct chemical-bond tomography from a diamond–graphite phantom specimen. a, Schematic computer reproduction of the sample. **b**, Diffraction contrast measurement of the full volume. **c**, Fingerprint spectra measured from a highly oriented pyrolythic graphite and diamond powder. To determine the bonding characteristics and orientation, it suffices to measure spectra at the two labelled energies E_a and E_b (see text). **d**, Spectra for $S(\mathbf{Q}, E, x)$ through the graphite–diamond ensemble, for the beam path shown in Fig. 3a. **e**, Chemical-bond contrast 3D image in a selected region around the diamond corner. Isosurfaces correspond to diamond-like carbon (red) and graphite with an orientation $\mathbf{Q} \parallel ab$, that is, with the sp^2 bond in the xy plane (blue).

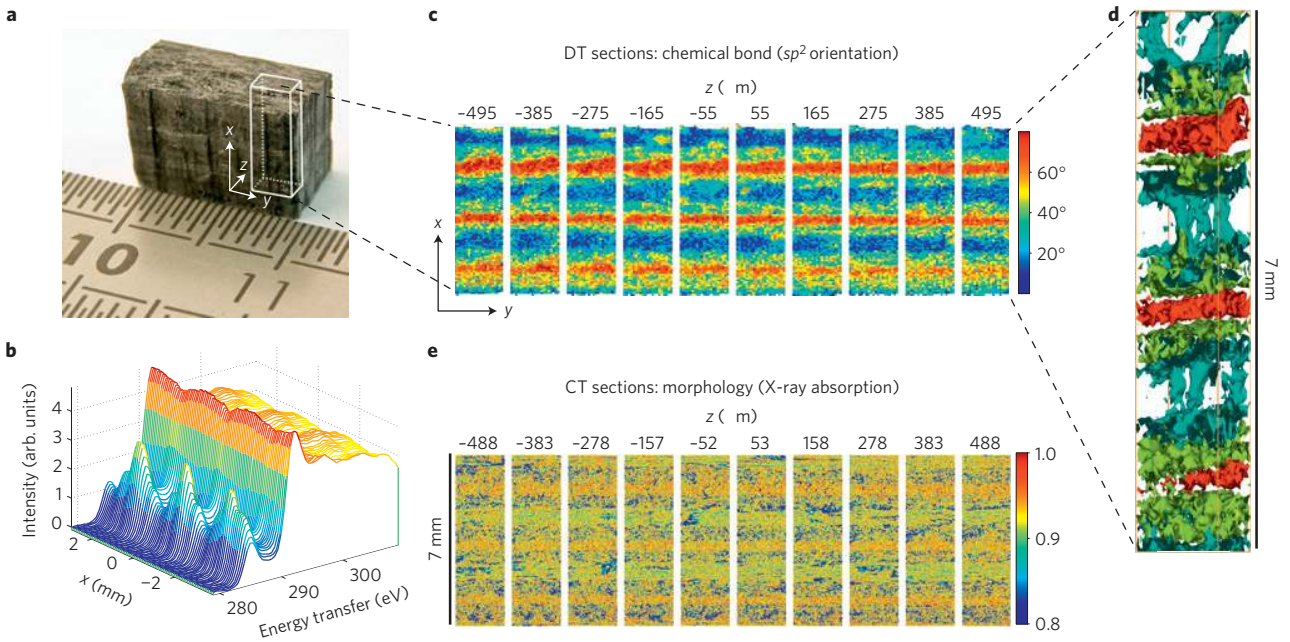

Figure 4 | Application of direct tomography to a layered C/SiC sample. a, Photograph of the sample. **b**, Carbon near-*K*-edge XRS spectra as a function of the beam propagation direction *x*, showing the ABCBA-periodicity of the spectra. **c**, The orientation of the sp^2 bond plane determined with respect to **Q**. Here we show *xy* sections for different values of *z* of a $7 \times 2 \times 1\,\mathrm{mm}^3$ subvolume within the sample. **d**, Same as **c** but as a 3D isosurface plot for selected angles (colour map the same as in **c**). **e**, Same as **c** but measured with absorption-contrast CT, revealing the corresponding variations in sample density.

two characteristic energies ($E_a = 285\,\mathrm{eV}$, the energy of the π^* exciton, and $E_b = 288\,\mathrm{eV}$, the rising edge of the main line) suffices to yield the bond character. In Fig. 3d we show a 1D pathway piercing through the sample with the resulting C *K*-edge XRS spectrum $S(\mathbf{Q}, E, x)$. We measured $S(\mathbf{Q}, E, x, y, z)$ in this 1D piercing mode around one corner of the diamond, and assigned $S(\mathbf{Q}, E_b, x, y, z) - S(\mathbf{Q}, E_a, x, y, z)$ as the value corresponding to each measured voxel. The resulting isosurfaces are shown in Fig. 3e, at a characteristic value for diamond, and at a value corresponding to graphite with $\mathbf{Q} \parallel ab$. The pellet was compressed from graphite powder, with the compression axis along *z*, using a pressure of 250 MPa. The resulting graphite was thus highly oriented, with the sp^2 bonds in the *xy* plane, which is also the plane of the **Q** vector defined by the laboratory coordinates. The fuzziness of the *ab*-orientation isosurface results from the remaining small variations from a perfect in-plane orientation. The spatial resolution here is 30 μm in the *y* and *z* directions, and 150 μm in *x*. This demonstration using a phantom sample shows that DT is able to determine the chemical bond of carbon, in 3D, embedded several millimetres inside another form of carbon, from the spectral signature of the chemical bond.

As an example of a sample relevant to materials science we used a specimen of carbon fibre-reinforced silicon carbide (C/SiC). The material is well known for retaining its mechanical properties even above 2,000 K. Figure 4a shows a photograph of the sample, which was an approximately $7 \times 10 \times 5\,\mathrm{mm}^3$ cuboid. Figure 4b shows the carbon *K*-edge XRS spectra $S(\mathbf{Q}, E, x)$, which reveal the bonding characteristics within the sample thickness of 7 mm. Comparing the spectra to the fingerprint standards of Fig. 3c reveals that because the π^* exciton is visible for all *x*, the sp^2 bond dominates, the bond orientation varying in an approximately layered ABCBA structure. We then proceeded with a measurement over all three spatial dimensions of $S(\mathbf{Q}, E, x, y, z)$ in a $7 \times 2 \times 1\,\mathrm{mm}^3$ subvolume. To visualize the result, we determined the average bond orientation as the angle between the sp^2 plane and the **Q** vector, and assigned it as the value of the corresponding voxel. The resulting volume is visualized in certain selected 2D *xy* sections in Fig. 4c, and in a series of isosurfaces for selected values in Fig. 4d. To demonstrate the unique contrast in DT, in Fig. 4e we show the same sections as in Fig. 4c, but determined using state-of-the-art microtomography (μCT). This technique can determine the effective density of the material with very high spatial resolution, resolving even fibrous microstructure, but is less sensitive to the overall layered structure because of the relatively small variations in density. The elemental composition of the sample is obviously not determined by μCT at all, let alone the chemical bond variations. In contrast, the DT data set in Fig. 4c–d implies a determination of (1) the carbon distribution within the sample and (2) its average chemical bond within each voxel. In this particular case, we found sp^2 carbon dominating within the measured volume and could determine the bond orientation variations. As a result, DT is able to determine the nature of the layered structure at the molecular level. These data thus show a novel way to resolve the chemical bond variations of low-*Z* elements in the deep bulk and in 3D.

The direct tomography method that we have developed uses hard-X-ray scattering, both elastic and inelastic, as contrast mechanisms. The novel aspects are that this dark-field imaging technique works directly in Cartesian space without involving any rotations, and that the contrast mechanism is sensitive to the chemical bond. The technique is especially interesting in the studies of the local structure and chemical bond of low-*Z* elements, which are otherwise largely inaccessible. Examples of applications of this *in situ* chemical 3D imaging include polymerization, topochemical reactions, chemical reactions (even in hostile environments such as nanoparticle formation in supercritical water), *in operando* battery electrodes, fuel cells, liquid inclusions in solid materials, and so on. There is great promise for the technique as a characterization method and an analytical tool for materials science, engineering, physics, chemistry and biology.

Methods

We used the beamline ID16 of the European Synchrotron Radiation Facility (Grenoble, France)[27]. The incident radiation from three consecutive undulators was monochromated by a Si(111) double-crystal monochromator to 1.5-eV bandwidth, the photon energy being ~13 keV (wavelength 0.96 Å). The incident

beam was focused either by a cylindrical mirror horizontally (y direction) to 100 μm, the vertical beam size being 1 mm; or by a toroidal mirror to $30 \times 100\,\mu m^2$ ($z \times y$), further slitting down to $30 \times 30\,\mu m^2$. The spectrometer consisted of a spherically bent Si(880) wafer with a diameter of 100 mm and surface curvature radius 1,000 mm. The total energy resolution was 2.5 eV full-width at half-maximum. The detector was a Medipix2 hybrid pixel detector based on a 256×256 pixel matrix with a 300 μm thick Si chip. The pixel size of the detector was 55 μm square.

IXS spectroscopy measures the probability of a photon-in–photon-out process, in which a hard X-ray photon loses part of its energy E_1 to an excitation of energy E, leaving the sample with a slightly diminished energy $E_2 = E_1 - E$. Both E_1 and E_2 are in the hard X-ray range, typically between 10 and 20 keV, and energy transfers E are usually limited to $\lesssim$1 keV. Note that there are no soft X-rays involved. It is the energy transfer E that determines the type of the studied excitation—in the case of XRS from a carbon K electron, $E \sim 290$ eV. It is the fact that only hard X-rays are involved for both the in- and outgoing radiation that allows bulk-sensitive studies such as the one described in this Letter. For $E_1 = E_2$, a condition which is easy to achieve, scattering is elastic and the measurement corresponds to diffraction (from crystals) or diffuse scattering (from weakly ordered materials). In the measurement, we keep E_2 fixed and tune E_1 instead, thus changing the value of E to perform energy scans. The scanning mesh of the sample position over the required Cartesian dimensions was done using the step size of the beam width (full-width at half-maximum).

The detector images in DT correspond directly to xz section images or x-direction pathways in the 2D sectioning mode or in the 1D piercing mode, respectively. The acquired raw data were combined to yield four-dimensional matrices with the dimensions corresponding to E, x, y and z, using the Matlab software (version 7.10, MathWorks, 2010) with custom-written analysis routines. As the technique is a direct tomography, no reconstruction algorithms are required. The acquired images were simply stacked as layers of the matrix. Each voxel contains a channel that represents the IXS spectrum. These spectra were background subtracted and area-normalized. The line integral of absorption to and from a voxel's location in the sample naturally affects the overall intensity of the spectra contained in that voxel. However, as long as the acquired statistical accuracy for that voxel is sufficient, the spectra can always be brought into absolute scale. Thus self-absorption effects are accounted for implicitly by the analysis. We used the Matlab Sliceomatic package (E. Ludlam, Matlab Central) and Avizo 6.3 (VSG) for 3D data visualization. The X-ray microtomography (μCT) of Fig. 4e was measured at the Laboratory of Microtomography of the University of Helsinki, Finland, using a state-of-the-art μCT scanner, nanotom(R), supplied by Phoenix X-Ray Systems + Services GmbH.

The exposures and scanning required 1 h for the diffraction-contrast image of Fig. 3b, 8 h for the chemical-bond DT of Fig. 3e, and 17 h for the data in Fig. 4c,d. One analyser crystal was used in the detection, covering 0.06% of the 4π solid angle. Increasing the data collection efficiency is possible: IXS spectrometers installed at synchrotron radiation sources are already capable of increasing the efficiency by an order of magnitude[27–29] and upgrades are planned aiming at an ~100-fold higher efficiency in near future. The spatial resolution is determined by the incident-beam optics in at least one Cartesian dimension (y, and in the 1D piercing mode also in z). The resolution in the remaining dimensions (at least x, and in the 2D sectioning mode also in z) is given by the analyser crystal focus. As inelastic scattering spectroscopy is, in general, photon-hungry, the optics used should operate at as high an efficiency as possible. Kirkpatrick–Baez optics at hard X-ray energies (>10 keV) can perform in the resolution range of 10 μm without loss of flux. With certain sacrifices in efficiency, focusing capabilities have been demonstrated below 100 nm (ref. 30). The analyser crystals can currently perform in the sub-100-μm resolution range and improvements to go below this are being made. The useful overall resolution range is foreseen to be of the order of 10 μm.

Received 16 December 2010; accepted 19 April 2011; published online 29 May 2011

References

1. Larson, B. C., Yang, W., Ice, G. E., Budai, J. D. & Tischler, J. Z. Three-dimensional X-ray structural microscopy with submicrometre resolution. *Nature* **415,** 887–890 (2002).
2. Schmidt, S. *et al.* Watching the growth of bulk grains during recrystallization of deformed metals. *Science* **305,** 229–232 (2004).
3. Jensen, D. J. *et al.* X-ray microscopy in four dimensions. *Mater. Today* **9,** 18–25 (2006).
4. Bleuet, P. *et al.* Probing the structure of heterogeneous diluted materials by diffraction tomography. *Nature Mater.* **7,** 468–472 (2008).
5. Levine, L. E. & Long, G. G. X-ray imaging with ultra-small-angle X-ray scattering as a contrast mechanism. *J. Appl. Cryst.* **37,** 757–765 (2004).
6. Schroer, C. G. *et al.* Mapping the local nanostructure inside a specimen by tomographic small-angle X-ray scattering. *Appl. Phys. Lett.* **88,** 164102 (2006).
7. Pfeiffer, F. *et al.* Hard-X-ray dark-field imaging using a grating interferometer. *Nature Mater.* **7,** 134–137 (2008).
8. Chapman, D. *et al.* Diffraction enhanced X-ray imaging. *Phys. Med. Biol.* **42,** 2015–2025 (1997).
9. Bravin, A. Exploiting the X-ray refraction contrast with an analyser: The state of the art. *J. Phys. D* **36,** A24–A29 (2003).
10. Fernández, M. *et al.* Human breast cancer *in vitro*: Matching histo-pathology with small-angle X-ray scattering and diffraction enhanced X-ray imaging. *Phys. Med. Biol.* **50,** 2991–3006 (2005).
11. Davis, T. J., Gao, D., Gureyev, T. E., Stevenson, A. W. & Wilkins, S. W. Phase-contrast imaging of weakly absorbing materials using hard X-rays. *Nature* **373,** 595–598 (1995).
12. Wilkins, S. W., Gureyev, T. E., Gao, D., Pogany, A. & Stevenson, A. W. Phase-contrast imaging using polychromatic hard X-rays. *Nature* **384,** 335–338 (1996).
13. Snigirev, A., Snigireva, I., Kohn, V., Kuznetsov, S. & Schelokov, I. On the possibilities of X-ray phase contrast microimaging by coherent high-energy synchrotron radiation. *Rev. Sci. Instrum.* **66,** 5486–5492 (1995).
14. Pfeiffer, F., Weitkamp, T., Bunk, O. & David, C. Phase retrieval and differential phase-contrast imaging with low-brilliance X-ray sources. *Nature Phys.* **2,** 258–261 (2006).
15. Ade, H. *et al.* Chemical contrast in X-ray microscopy and spatially resolved XANES microscopy of organic specimens. *Science* **258,** 972–975 (1992).
16. Schroer, C. G. *et al.* Mapping the chemical states of an element inside a sample using tomographic X-ray absorption spectroscopy. *Appl. Phys. Lett.* **82,** 3360–3362 (2003).
17. Golosio, B. *et al.* Nondestructive three-dimensional elemental microanalysis by combined helical X-ray microtomographies. *Appl. Phys. Lett.* **84,** 2199–2201 (2004).
18. Pascarelli, S., Mathon, O., Muñoz, M., Mairs, T. & Susini, J. Energy-dispersive absorption spectroscopy for hard-X-ray micro-XAS applications. *J. Synchrotron Radiat.* **13,** 351–358 (2006).
19. Ade, H. & Stoll, H. Near-edge X-ray absorption fine-structure microscopy of organic and magnetic materials. *Nature Mater.* **8,** 281–290 (2009).
20. Schülke, W. *Electron Dynamics by Inelastic X-Ray Scattering* (Oxford Univ. Press, 2007).
21. Shvyd'ko, Y. V., Stoupin, S., Cunsolo, A., Said, A. H. & Huang, X. High-reflectivity high-resolution X-ray crystal optics with diamonds. *Nature Phys.* **6,** 196–199 (2010).
22. Hart, M. Synchrotron radiation—its application to high-speed, high-resolution X-ray-diffraction topography. *J. Appl. Cryst.* **8,** 436–444 (1975).
23. Baruchel, J. *et al.* Phase imaging using highly coherent X-rays: Radiography, tomography, diffraction topography. *J. Synchrotron Rad.* **7,** 196–201 (2000).
24. Mao, W. L. *et al.* Bonding changes in compressed superhard graphite. *Science* **302,** 425–427 (2003).
25. Meng, Y. *et al.* The formation of sp^3 bonding in compressed BN. *Nature Mater.* **3,** 111–114 (2004).
26. Lee, S. K. *et al.* Probing of bonding changes in B_2O_3 glasses at high pressure with inelastic X-ray scattering. *Nature Mater.* **4,** 851–854 (2005).
27. Verbeni, R. *et al.* Multiple-element spectrometer for non-resonant inelastic X-ray spectroscopy of electronic excitations. *J. Synchrotron Rad.* **16,** 469–476 (2009).
28. Cai, Y. Q. *et al.* Optical design and performance of the Taiwan inelastic X-ray scattering beamline (BL12XU) at SPring-8. *AIP Conf. Proc.* **705,** 340–343 (2004).
29. Fister, T. T. *et al.* Multielement spectrometer for efficient measurement of the momentum transfer dependence of inelastic X-ray scattering. *Rev. Sci. Instrum.* **77,** 063901 (2006).
30. Hignette, O., Cloetens, P., Rostaing, G., Bernard, P. & Morawe, C. Efficient sub 100 nm focusing of hard X rays. *Rev. Sci. Instrum* **76,** 063709 (2005).

Acknowledgements

The authors would like to thank L. Simonelli, V. Giordano, G. Vankó, H. Suhonen, A. Kallonen, C. Henriquet, C. Ponchut, and T. Ahlgren for their support, help, and invaluable discussions. T.P. and K.H. were supported by the Academy of Finland under the contract 1127462, and S.H. by University of Helsinki research funds (project 490076).

Author contributions

S.H., T.P., R.V., G.M. and K.H. designed and carried out the experiments and wrote the paper; S.H. and T.P. analysed the data.

Additional information

The authors declare no competing financial interests. Reprints and permissions information is available online at http://www.nature.com/reprints. Correspondence and requests for materials should be addressed to S.H.